Ocean Dynamics (2011) 61:525–541
DOI 10.1007/s10236-011-0377-8

Estimate of eddy energy generation/dissipation rate in the world ocean from altimetry data

Chi Xu · Xiao-Dong Shang · Rui Xin Huang

Received: 18 June 2010 / Accepted: 5 January 2011 / Published online: 3 February 2011

Abstract Assuming eddy kinetic energy is equally partitioned between the barotropic mode and the first baroclinic mode and using the weekly TOPEX/ERS merged data for the period of 1993~2007, the mean eddy kinetic energy and eddy available gravitational potential energy in the world oceans are estimated at 0.157 and 0.224 EJ; the annual mean generation/dissipation rate of eddy kinetic energy and available gravitational potential energy in the world oceans is estimated at 0.203 TW. Scaling and data analysis indicate that eddy available gravitational potential energy and its generation/dissipation rate are larger than those of eddy kinetic energy.

High rate of eddy energy generation/dissipation is primarily concentrated in eddy-rich regions, such as the Antarctic Circumpolar Current and the western boundary current extensions. Outside of these regimes of intense current, the energy generation/dissipation rate is two to four orders of magnitude lower than the peak values; however, along the eastern boundaries and in the region where complicated topography and current interact the eddy energy generation/dissipation rate is several times larger than those in background.

Responsible Editor: Steve Rintoul

C. Xu · X.-D. Shang (✉)
Key Laboratory of Tropical Marine Environmental Dynamics,
South China Sea Institute of Oceanology,
Chinese Academy of Sciences,
Guangzhou 510301, China
e-mail: xdshang@scsio.ac.cn

R. X. Huang
Woods Hole Oceanographic Institution,
Woods Hole, MA 02543, USA

C. Xu
Graduate University of Chinese Academy of Sciences,
Beijing 100049, China

Keywords Mesoscale eddies · Altimetry data · Generation/dissipation rate · Two-layer model

1 Introduction

Eddies are the most important component of the oceanic circulation. Scale analysis indicates that eddy kinetic energy (EKE) is two orders of magnitude larger than the mean flow kinetic energy, and eddy available potential energy is one order of magnitude larger than EKE (Gill et al. 1974; Huang 2010). Satellite altimetry data analysis indicates that at least on the sea surface of the subtropical gyres, EKE is indeed about 100 times larger than the mean flow kinetic energy; however, this ratio is reduced to approximately ten in most part of the Antarctic Circumpolar Current (ACC) (Wunsch 2007, plate 6). EKE is most contained in the form of geostrophic (or mesoscale) eddies on scales of 50 to 100 km and time scale of 10~100 days; these eddies dominate the oceanic kinetic energy at sub-inertial frequencies at mid- and high latitudes (Ferrari and Wunsch 2009). However, it is clear that at this time we have no reliable theory and data for eddy energy generation/dissipation rate in the world oceans. Since this is a critically important component of the global energy budget, a clear dynamical picture and a detailed balance are most desirable. Hence, we postulate a method to combine altimetry data with a hydrographic climatology; this method can provide useful information about the size of eddy-related energy reservoirs, including potential and kinetic energy, in the world ocean, and the associated conversion rates.

It has been long recognized that mesoscale eddies play important roles in the energetics of the global oceans. In the 1970s, the first international field program POLYMODE aimed at observing mesoscale eddies in the oceans was organized

(Gould et al. 1974). Despite grand technique challenges associated with observing eddies in the oceans, much progress was made. In particular, regimes of high values of EKE in the Gulf Stream extension, the Kuroshio extension and the ACC were identified (Wyrtki et al. 1976; Richardson 1983). With the advance of satellite altimetry in 1990s, nearly synoptical global pictures of the EKE distribution (Cheney et al. 1983; Zlotnicki et al. 1989; Shum et al. 1990; Stammer 1997; Ducet et al. 2000) are provided. With the improvement in remote sensing technique and accumulation of data, more precise pictures of the spatial structure and temporal evolution of the eddy field are immerging.

Most previous studies have been primarily focused on EKE, often calculated as half of the squared geostrophic velocity. In a stratified fluid, both the kinetic energy and available gravitational potential energy (AGPE) are important. Scaling indicates that most of the eddy energy may be stored in the form of eddy available gravitational potential energy (EAGPE), which is defined as the difference in gravitational potential energy between a reference state and the physical state associated with an eddy. However, this aspect of eddy energetics has not received much due attention.

As discussed in Feng et al. (2006), the AGPE is very sensitive to the choice of the reference state. For a person walking on a flat land, his AGPE seems rather small. However, when he sees a deep well by the road side, he realizes that his AGPE can be huge in comparing with the bottom of the well. Early studies of basin-scale AGPE by Oort et al. (1994) was based on a reference state obtained by horizontally averaging the global stratification. Such a formulation is, however, not suitable for the study of basin-scale circulation. A more suitable definition derived from the original definition of available potential energy should be used, and a computational algorithm including the compressibility of seawater and realistic topography was developed by Huang (2005, 2010). On the other hand, for the study of mesoscale eddies in the oceans, the locally averaged stratification can be used as the reference state. Accordingly, the EAGPE in the world oceans was estimated at 1–8 EJ (1 EJ=10^{18} J, Feng et al. 2006). Furthermore, the global distribution of EAGPE is closely linked to the strong density fronts and currents in the oceans, implying that baroclinic instability could be the major mechanism and energy source supporting these regimes of high EAGPE. In the present study, we use a two-layer model to study the structure of an eddy; the reference state is defined as the state with no free surface elevation caused by eddy. The appropriate EAGPE algorithm can be derived from such a simple layer model.

Mesoscale eddies in the ocean evolve with time through the following processes: eddy generation through baroclinic/barotropic instability or directly forced by wind perturbations; energy transfer through eddy–eddy interaction and eddy-mean flow interaction; and finally through many dynamic processes eddies lose their energy and eventually die.

The generation of eddies in the oceans may be linked to both the atmospheric forcing and the instability in the oceans. Frankignoul and Muller (1979) postulated that mesoscale eddies were mainly forced by the fluctuating winds; they put the energy source due to atmospheric forcing at 0.05 TW. Comparing this level of energy source with other sources, wind fluctuations do not seem to play a dominant role (Wyrtki et al. 1976; Stammer et al. 2001).

The other source of eddy has been identified as the instability in the oceans, including both baroclinic and barotropic instability. These dynamical processes have been studied extensively and summarized in textbooks, (Pedlosky 1987). Observations confirmed the claim of instability theory. For example, Stammer (1997) found eddy variability was positively correlated with the mean horizontal density gradients; thus, the internal instability is a primary source of eddy because large horizontal density gradient means strong baroclinic instability. Hydrographic data analysis indicated that the ocean is baroclinically unstable everywhere (Smith 2007; Killworth and Blundell 2007), suggesting the source of eddy energy is available in the oceans. Hence, the release of potential energy through baroclinic instability can be a major mechanism sustaining the generation of mesoscale eddies.

How much eddy energy is actually generated through baroclinic instability? Using the commonly accepted Gent–McWilliams scheme, Huang and Wang (2003) made an attempt of estimate the conversion rate from the mean-state gravitational potential energy to eddy energy. Since eddy parameterization remains a crude numerical technique, the conversion rate is rather sensitive to the choice of parameter. A close examination was taken by Wunsch and Ferrari (2004), and they put the estimate at 0.2~0.8 TW. In a more recent review, Ferrari and Wunsch (2009) put this conservation rate at 0.3 TW.

Obviously, the conversion rate is limited by the rate of wind energy input to the surface current; the estimate of this rate is 0.85~1 TW according to the studies by Wunsch (1998), Huang et al. (2006), and the most recent study by Scott and Xu (2009). Thus, the eddy energy generation rate should be a fraction of 1 TW. However, due to the limitation of in situ observations and computer power, no reliable estimate of this rate has been published so far.

Another question is how eddies lose their energy. Due to the limitation of in situ observations and computer power, we have no clear dynamic picture for this critically important component of the world ocean energetics.

Eddies may lose their energy through the following processes: bottom drag, loss of balance (or called surface frontogenesis which results from eddy stirring and implies an energy cascade from the first baroclinic mode to scales smaller than the first deformation radius), interactions with the internal wave field, continental margin scattering/absorption and suppression by wind work. Some of these processes were briefly discussed by Ferrari and Wunsch (2009); however, most of these items remain unexplored.

Some observation data suggested that eddy dissipation is closely linked to rough topography, e.g., current meter record study by Fu et al. (1982), altimeter data analysis by Gille at al. (2000) and model study by Arbic and Flierl (2004). Wunsch and Ferrari (2004) estimated this rate of energy loss at 0.4 TW. Using moored current meter records and altimetry data, Sen et al. (2008) reexamined the bottom drag and suggested that the global dissipation rate of low-frequency flow by quadratic bottom boundary layer drag falls within the range of 0.2 to 0.8 TW. Based on high-resolution global simulations, Arbic et al. (2009) put the global dissipation rates by quadratic bottom boundary layer drag at 0.14 to 0.65 TW. Although these studies seem to give a rather high upper limit for the rate of eddy energy dissipation through bottom friction, it is questionable whether bottom friction can take up such a large portion of the total eddy energy.

Although the eddy-related energy and conversion rates are critically important, progress in diagnosis based on observation data has been rather slow. Satellite altimetry is the most powerful tool currently available in collecting synoptic data of eddy-related sea surface height anomaly on global scale. In order to incorporate the vertical structure of eddies, the simplest approach is to use a two-layer model to infer the baroclinic structure of eddies. Thus, our study is focused on the diagnosis of eddy energy generation/dissipation rates based on reliable merged satellite altimetry data and an equivalent two-layer model.

In section 2, we discuss the calculation of the EKE and the EAGPE based on the framework presented in appendixes for a two-layer model and an equivalent two-layer model (EQ-model hereafter; Flierl 1978). Accordingly, eddy energy can be linked to the free surface elevation anomaly from satellite data. In section 3, the data analysis methods are presented. The results of our analysis are presented in section 4, and finally, conclusions are in section 5.

2 Two-layer model and calculation algorithms

Mesoscale eddy energy consists of two parts: EKE and EAGPE. Eddies can be classified as barotropic eddy, baroclinic eddy of mode 1, mode 2, and so on. In theory, eddy energy calculation should include contribution from all possible modes. However, such a calculation requires information about the vertical structure of eddies, which is not available from satellite altimetry data.

Wunsch (1997) went through a detailed analysis for all current meter data available at that time, and his results indicated that most part of eddy kinetic energy is contained in the first baroclinic mode. Forget and Wunsch (2007) analyzed all hydrographic data in the global oceans and came to a similar conclusion: “Over the global ocean, the interpretation of the SSH variability as the vertical displacement signature of the first baroclinic mode is a reasonable approximation.” Ferrari and Wunsch (2010) noted that at periods beyond 1 day, kinetic energy of a water column is roughly equally partitioned between the barotropic mode and the first baroclinic mode. Thus, we will use this as a working assumption.

2.1 Model formulation

Before calculating eddy energy generation/dissipation rates, we present the formulations based on a two-layer model and an equivalent two-layer model inferred from a continuously stratified model. The details of model formulations are presented as follows: a two-layer model is presented in Appendix 1. An equivalent two-layer model inferred from a continuously stratified model, following Flierl (1978), is presented in Appendix 2, where the reason why this model is better than the traditional two-layer model, which is using the main pycnocline (thermocline) as the interface, is presented.

2.2 The calculation of the EKE and the EAGPE

Using the central difference scheme, the geostrophic velocities in the upper layer were computed from the sea surface height anomaly (SSHA) as $u_1 = -g\eta_y/f$ and $v_1 = g\eta_x/f$. Assume there are n grid points within the closed sea surface height anomaly contour of an eddy, the mean geostrophic velocity $\langle V_1 \rangle$ in the upper layer of the eddy is

$$< V_1 >= \sum_{i=1}^{n} \left(\sqrt{{u_{1,i}}^2 + {v_{1,i}}^2} \right) / n. \quad (1)$$

The total geostrophic kinetic energy of each eddy is

$$\mathrm{EKE} = \sum_{i=1}^{n} 0.5 (\nabla \eta_i / f)^2 \rho A_i H_{1,i} H_i / H_{2,i}, \quad (2)$$

where $\rho \approx 1,030\mathrm{kg/m}^3$is the reference density $H_{1,i}, H_{2,i}$are the upper, lower layer thickness and $H_i = H_{1,i} + H_{2,i}$is the total thickness at grid i.

From Eqs. 17 and 30, the corresponding formula for the EAGPE is

$$\mathrm{EAGPE} = \sum_{i=1}^{n} \overline{\rho} g \eta_i^2 \left(H_i/H_{2,i}\right)^2 A_i/2\varepsilon_i. \quad (3)$$

Our discussion above is focused on the first baroclinic mode. In general, eddy energy can exist in quite different forms. As discussed by Ferrari and Wunsch (2010), eddy motions in the ocean can be described in terms of the Quasi-Geostrophic (QG) modes in the oceanic interior, plus the so-called Surface Quasi-Geostrophic solutions (Lapeyre 2009). Since the traditional QG modes are defined for the ocean at rest, it is may not be the best way to represent motions observed in the ocean. On the other hand, the traditional QG modes are defined from the unforced solutions of the homogeneous Sturm–Liouville system, and these modes form an orthogonal and complete base; thus, any function has a unique (and convergent) expression in this base. Hence, we can use these modes as the base and assume that the eddy energy is partitioned as follows

$$E = c_0 E_{bt} + c_1 E_{bc,1} + c_2 E_{bc,2} + \ldots. \quad (4)$$

In this study, our focus is on the first two terms only; accordingly, the SSHA signals are separated into two parts

$$\eta = \eta_{bt} + \eta_{bc}, \eta_{bt} = \alpha\eta, \eta_{bc} = (1-\alpha)\eta, \quad (5)$$

where η_{bt} and η_{bc} are the barotropic and baroclinic components, and $\alpha \in [0, 1]$ is the fraction. To choose this fraction we assume that the total kinetic energy partition can be written as

$$\mathrm{ke} = \mathrm{ke}_{bt} + \mathrm{ke}_{bc}, \mathrm{ke}_{bt} = c \cdot \mathrm{ke}, \mathrm{ke}_{bc} = (1-c)\mathrm{ke}. \quad (6)$$

For each grid, the vertically integrated kinetic energy is

$$\mathrm{ke}_{bc} = 0.5\overline{\rho} A_i (\nabla\eta_{bc}/f)^2 H_{1,i} H_i/H_{2,i}, \quad (7)$$

$$\mathrm{ke}_{bt} = 0.5\overline{\rho} A_i (\nabla\eta_{bt}/f)^2 H_i. \quad (8)$$

From Eqs. 5, 6, 7, and 8, we obtain

$$\alpha = \left(1 + \sqrt{\frac{H_{2,i}}{H_{1,i}} \frac{1-c}{c}}\right)^{-1}, \quad (9)$$

$$\mathrm{EKE} = \sum_{i=1}^{n} (1-\alpha)^2 \overline{\rho} A_i (\nabla\eta_i/f)^2 H_{1,i} H_i/H_{2,i}. \quad (10)$$

The available gravitational potential energy associated with the barotropic mode is much smaller than the corresponding kinetic energy, thus can be omitted; the available gravitational potential energy for an eddy is

$$\mathrm{EAGPE} = \sum_{i=1}^{n} (1-\alpha)^2 \overline{\rho} g \eta_i^2 \left(H_i/H_{2,i}\right)^2 A_i/2\varepsilon_i. \quad (11)$$

On the sea surface, the percentage of the kinetic energy associated with the first baroclinic mode is

$$R_{bc} = (1-\alpha)^2 / \left[\alpha^2 + (1-\alpha)^2\right]. \quad (12)$$

It is clear that c may be a function of space and time; however, as a first step in revealing the eddy energetics, we will assume $c=0.5$ is a global constant, i.e., the water-column-integrated kinetic energy is equally partitioned between the barotropic mode and the first baroclinic mode; thus, we have

$$R_{bc} = H_2/H. \quad (13)$$

Since the upper layer is much thinner than the lower layer, the surface kinetic energy is mostly associated with the first baroclinic mode, as discussed by Wunsch (1997). In the following discussion, we will present results based on the case with $c=0.5$, unless stated otherwise.

3 Data analysis

3.1 The data

The weekly TOPEX/ERS merged data over period 1993~2007 were used in our analysis. We used the data covers the latitude band from 60° S to 60° N with a horizontal average resolution of 0.333×0.265°. Since errors of altimeter data are larger near the boundary, the SSHA data over regimes with depth shallower than 200 m are abandoned. Many issues related to the quality and utility of this data set have been discussed in previous studies, e.g., Chelton et al. (2007a).

The stratification data is obtained from the WOA01 annual mean climatology of temperature and salinity. The vertical structure of T and S profiles at each 1×1° grid point is linearly interpolated to a vertically uniform grid of 50-m interval. The squared buoyancy frequency $N^2(z)$ at each grid is calculated by the standard Matlab subroutine: Seawater (provided by CSIRO MatLAB Seawater Library, Phil Morgan, CMR).

3.2 Identifying and tracking mesoscale eddies

Eddy-like character of variability (time scales of 100 days and space scales of 100 km) can be identified from SSHA as follows. Firstly, the SSHA fields were zonally high-pass filtered to remove large-scale heating and cooling effects (Chelton and Schlax 1996). The resulting anomaly fields were high-pass filtered with filter cutoffs of $6\times6°$ to reduce mapping errors. The reasons of choosing high-pass filter are twofolds. In general, the size of an eddy is smaller than $6\times6°$, especially at high latitudes. In addition, at lower latitudes perturbations are primarily in the form of linear Rossby waves with relatively large spatial scale; thus, with high-pass filtering applied to remove the large-scale SSHA, only eddy signals are retained (Chelton et al. 2007b).

Two criteria applied to identify eddies. (1) A closed contour of SSHA with amplitude of at least ±5 cm and (2) the zonal and longitudinal spread of the area enclosed by SSHA contour are both at least 0.5°. The central location of the eddy is defined as the centroid of area within the closed SSHA contour. Since f approaches zero near the equator, the eddy calculation is limited to 5° off the equator.

Eddies are tracked from SSHA fields at consequent time steps as follows. If an eddy center at next step is located within a circle centralized at the center of an eddy at the previous time step, these two eddies are considered as the same eddy at these two time steps. To avoid jumping from one track to another, the radius of the circle is restricted to 1° of latitude.

Comparing eddy characteristics in our analysis with results from Chelton et al. (2007a) showed a good agreement in almost all important aspects, including the global distribution of eddies, and eddy propagation velocities and direction. The number of eddies in our results are slightly larger due to the fact that high-pass filtering enhances the eddy variability at higher spatial resolutions.

Analyzing the merged altimetry product over the 15-year data, approximately 275,000 eddies were identified and the number of long-lived cyclonic (anticyclonic) eddies with lifetime ≥4 weeks were 51,719 (51,557); thus, 37.55% of the observed eddies were long-lived. The trajectories, the number per 1° square of long-lived eddies and their mean EKE (per unit mass) derived from the geostrophic velocities are shown in Fig. 1.

Eddies are mainly concentrated in the vicinity of the major current systems. At low latitudes (especially the equatorial band), at high latitudes, and in the eastern basins eddy activity is much lower. Lack of eddies in these regimes may be due to the fact that large-scale ocean waves there may dominate the observed SSHA (Chelton et al. 2007b). Eddies in the tropics propagate mostly westward; while eddies in the western boundary current extensions have eastward velocity components, which may be induced by the mean flow. Eddies in the ACC band primarily propagate eastward due to the intense eastward current and the Westerly wind. The mean EKE (per unit mass) shown in the lower panels of Fig. 1 is directly calculated from the SSHA data. The pattern and strength of the EKE are in excellent agreement with Stammer (1997, his Fig. 2) and Ducet et al. (2000, their plate 8). In conclusion, thus, the distribution and directly derived energetics of mesoscale eddies are very similar with results in previous publications.

3.3 Calculation of the annual mean generation/dissipation rate of mesoscale eddies

Through eddy identification and tracking, the time series of position and energy for an eddy were obtained and the total energy of an eddy at each moment in its lifetime was calculated as summation of EKE and EAGPE.

Assume that we have a time series of an eddy, including its position and the SSHA at uniform time step of 1 week. In order to analyze the life cycle of the eddy, we extrapolate this life of eddy to define the beginning and end of the eddy. Eddy energy was first calculated in non-uniform grid points, and it was converted into a $1\times1°$ grid data set. The 15-year mean of sources/sinks at those grid points is thus computed (see detail in Appendix 3).

4 Results

4.1 The interfacial depth

The interfacial depth for the EQ-model can be determined by solving the eigen value problem and inferred from Eq. 37 in Appendix 2, Fig. 2a. In addition, this depth field is subjected to a constraint of $H_1 \leq H/2$ and a smoothing.

Alternatively, the corresponding interfacial depth of the thermocline model (TH-model) can be diagnosed from climatological data. After the approximate range is set, the level of maximum vertical temperature gradient in each station is diagnosed. For stations with no subsurface temperature gradient maximum, the corresponding depth is determined by interpolation from adjacent stations. The map after smoothing is shown in Fig. 2b.

At middle and low latitudes, these two maps share similar features. For example, the equivalent interface depth in the Atlantic is slightly larger than that in the Pacific Ocean and Indian Ocean. However, they are quite different at high latitudes. The upper layer thickness of the EQ-model is mostly deeper than 500 m poleward of 40°. Within the central latitude band of ACC, especially south of 45° S, the equivalent interface depth is on the order of 1,000 m. In comparison, the thermocline depth of the TH-model is quite shallow at high latitudes, on the order of 100–200 m only. In fact, the main thermocline outcrops along the poleward edge of the subtropical gyre. Thus, at latitudes higher than the poleward boundary of the subtropical gyres, there is no main thermocline or pycnocline. As a result, it is rather difficult to define such an interface, and the dynamical meaning of the TH-model seems unclear.

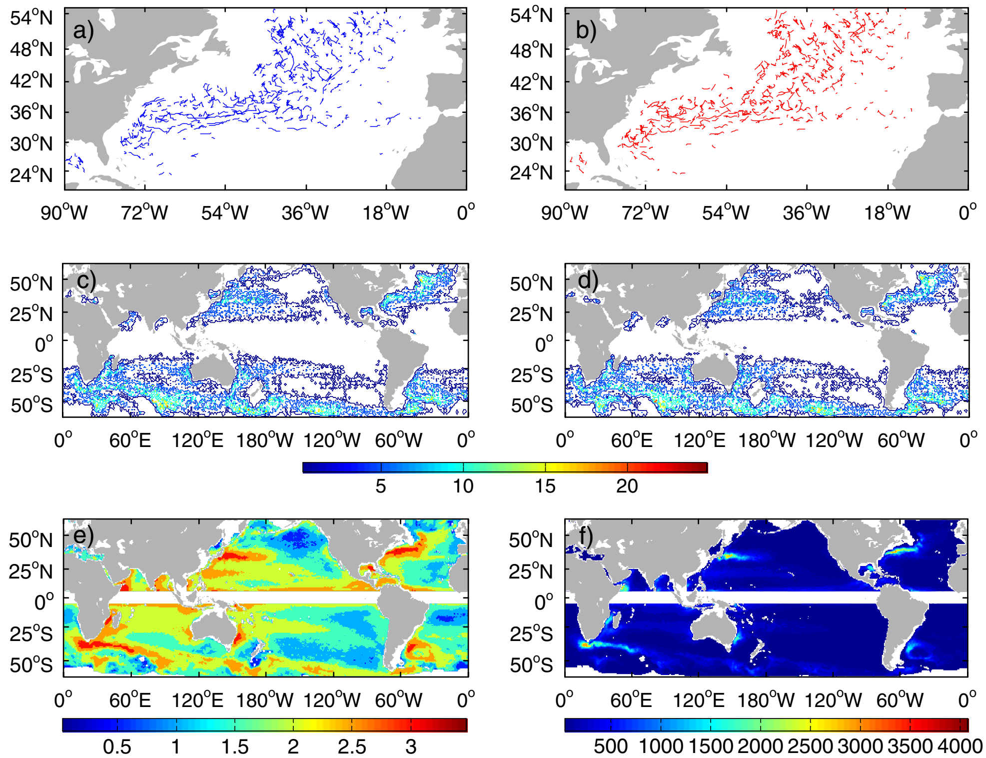

Fig. 1 *Top*, the trajectories of **a** cyclonic and **b** anticyclonic eddies with lifetimes≥4 weeks in North Atlantic in 1993. *Middle*, the number per 1° square of long-lived eddies in 15 years; **c** cyclonic eddies, and **d** anticyclonic eddies. The interval between contours is 5. *Bottom*, the global mean EKE (per unit mass) calculates as $0.5\times(u^2+v^2)$ in unit of $cm^2\ s^{-2}$, where u and v are zonal and meridional geostrophic velocities, respectively. **e** Plotted in $\log_{10}$ form; **f** plotted in linear scale

A close examination also reveals some difference exists at lower latitudes between these two models. For example, within 20° of the equator in the Pacific Ocean, the equivalent interfacial depth of the EQ-model is approximately 200 m, but it rises to 400 m in the east. On the other hand, the corresponding interfacial depth in the TH-model is deep in the western equatorial Pacific Ocean (150 m), but it is shallow in the eastern equatorial Pacific Ocean (less than 100 m). However, the difference in the equatorial band does not really affect our calculation in this study because the equatorial band turns out to be a zone of low eddy activity within our approach, as discussed above.

The density step ε for the EQ-model is calculated from Eq. 38, upper panel of Fig. 3. In compassion, the corresponding value for the TH-model is defined as: $\varepsilon' = (\overline{\rho_{\theta,\mathrm{lower}}} - \overline{\rho_{\theta,\mathrm{upper}}})/\rho$, where $\overline{\rho_{\theta,\mathrm{lower}}}$ and $\overline{\rho_{\theta,\mathrm{upper}}}$ are the mean potential density for the layers above and below the main thermocline at each station. The high-density step near the warm water pool in the equatorial Pacific reflects the fact that stratification is very strong due to the warm and relatively fresh water there. In comparison with the TH-model, density step obtained from the EQ-model is relatively large in the core of ACC. According to Eq. 33, this difference should give rise to a relatively low level of EAGPE. On the other hand, the equivalent interfacial depth of the EQ-model is much deeper in this area. According to Eq. 32, this should give rise to a much higher EKE there. The difference in these two models will be discussed further shortly. However, in the following analysis, we will use the equivalent interfacial depth and the density step inferred from the EQ-model, unless specifically stated otherwise.

4.2 The total EKE and EAGPE

We begin with the diagnoses of AGPE and EKE from satellite data. The meridional distributions of zonally integrated EKE/EAGPE for cyclonic eddies are shown in Fig. 4. Eddy activity in the equatorial band is very low, as shown in previous studies. In the Northern Hemisphere, high density of EKE and EAGPE appears around the latitude band of 40° N, which is closely related to the Gulf Stream and Kuroshio recirculation. In the Southern Hemisphere, there are two peaks. The northern peak around 40°S is related to the strong recirculation of the subtropical gyres, especially the Agulhas Return Current in the South Indian Ocean, and the confluence regimes of the subtropical gyre and the ACC. The second peak appears around 50°S, which is closely related to the strong eddy activity in connection with the core of the ACC.

In addition, the distribution of zonally mean eddy lifetime of cyclonic eddies is shown in Fig. 4c. There are two peaks of eddy lifetime in each hemisphere, and the global mean lifetime is about 4 weeks. Eddy lifetime gradually declines toward the equator. The reason of the eddy lifetime distribution remains unclear.

Both the ratio of EAGPE over EKE and the ratio of eddy scale over the radius of deformation vary greatly with

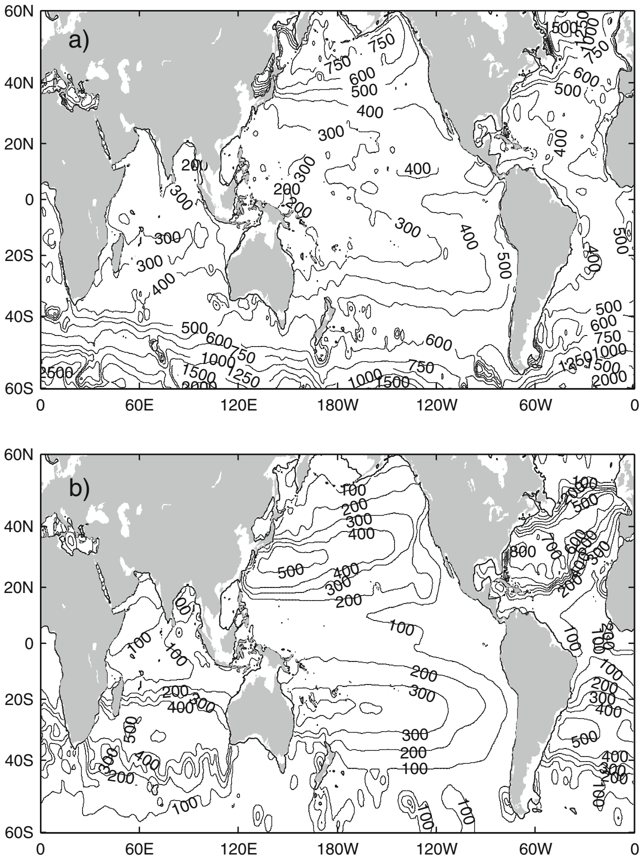

Fig. 2 The global map of **a** the equivalent interface depth H_1 of the equivalent two-layer model and **b** the depth of main thermocline, in meters. The *black heavy solid line* indicates the 200-m isobath, which marks the boundary of data domain

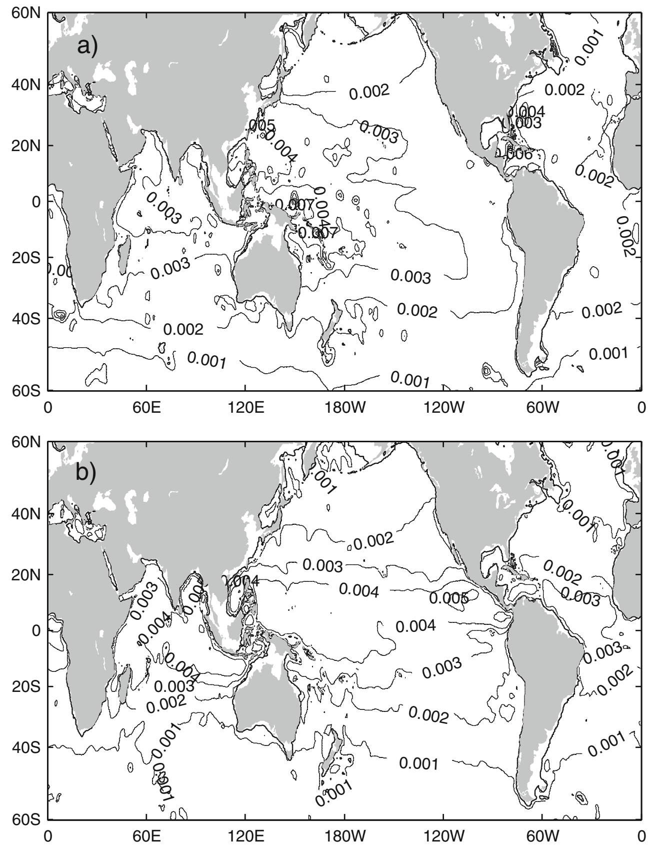

Fig. 3 The global map of **a** the density step $\varepsilon = g'/g$ derived from Eq. 38 and **b** the density step ε derived from the depth of main thermocline. It is dimensionless. The *black solid line* indicates the 200-m isobath, which marks the boundary of data domain

latitude, Fig. 4d. At lower latitudes, deformation radius is much larger than the mean eddy scale, and the energy ratio is smaller than one near the equator. At high latitudes, deformation radius is much smaller than the mean eddy scale, while the energy ratio is increased to 2 or even 3. This is consistent with the explanation and Eq. 34 in the Appendix 1 which implies the ratio of baroclinic EAGPE over baroclinic EKE is equal to the squared ratio of the eddy scale to the radius of deformation. According to Eq. 6, we have $\mathrm{k}e_{bc} = 0.5\mathrm{k}e$ and we omit the barotropic EAGPE in our calculation as mentioned in section 2.2, thus the ratio of baroclinic EAGPE over baroclinic EKE, indicated by the thin dashed line, is theoretically twice the ratio of EAGPE over EKE, depicted by the thin solid line. However, in Fig. 4d, on one hand, the squared ratio of the eddy scale to the radius of deformation (not shown) is lower than twice the ratio of EAGPE over EKE, suggesting that the eddy scale resolved from the SSHA fields may be underestimated. On the other hand, at mid-latitudes around 25° the energy ratio is larger than one while the radius ratio is smaller than one; we have not yet found any plausible explanation, and thus this is left for further study.

As shown in Fig. 5, regions of low energy ratio (no more than 2) are located within the subtropical gyre, including their western boundary and extensions where currents and eddy activity are quite strong. However, at high latitudes, especially in the east part of the North and South Pacific Ocean, the ratio is quite large where eddy generation is less active. The maximum ratio is larger than 10. At 45°S band, although the Rossby deformation radius is nearly the same, this ratio is quite large in the eastern part of the South Pacific and its conjunction with ACC, indicating that the spatial scale of eddies there is much larger than the deformation radius.

The total EKE/EAGPE diagnosed from the EQ-model is summarized and compared with previous estimates, Tables 1 and 2. The total EKE in cyclones (0.081 EJ) is slightly larger than that in anticyclones (0.076 EJ); similarly, the total EAGPE in cyclone (0.113 EJ) is slightly larger than that of anticyclones (0.111 EJ).

The total EKE and EAGPE is 0.157 and 0.224 EJ, respectively, Table 1. These values are much smaller than

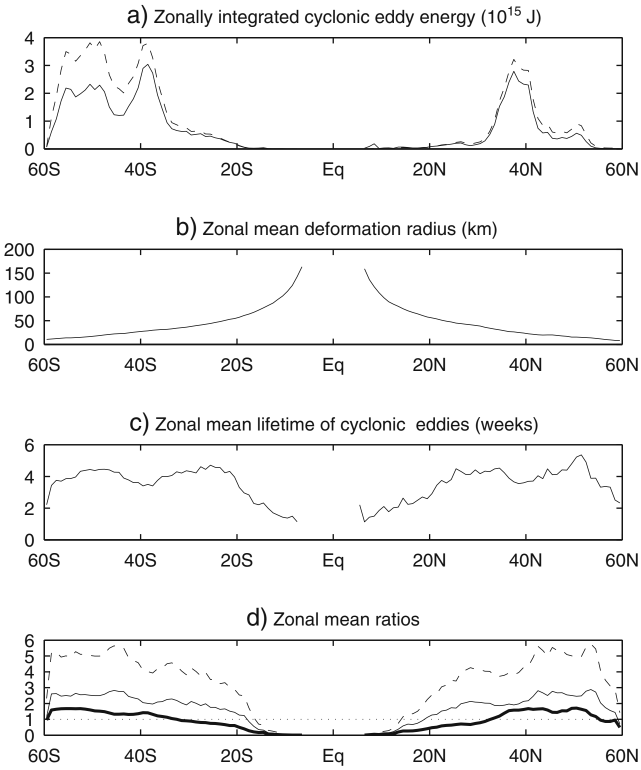

Fig. 4 Meridional distribution of eddy properties, based on the equivalent two-layer model. **a** Zonally integrated energy of cyclonic eddies. The *solid line* indicates the zonally integrated EKE while the *dashed line* indicates the zonally integrated EAGPE. **b** Zonal mean deformation radius. **c** Zonal mean lifetime of cyclonic eddies. **d** The *thick solid line* indicates the zonal mean ratio of eddy radius over the deformation radius. The *thin solid line* indicates the zonal mean ratio of EAGPE/EKE while the *thin dashed line* indicates twice the ratio of EAGPE/EKE. The *dotted line* indicates the ratios equal to 1

those reported in previous studies, Table 2. For example, using data for the monthly mean velocity for the period from 1958 to 2001 taken from Simple Ocean Data Assimilation (SODA) data (Carton and Giese, 2008), the mean kinetic energy of the world ocean is estimated at

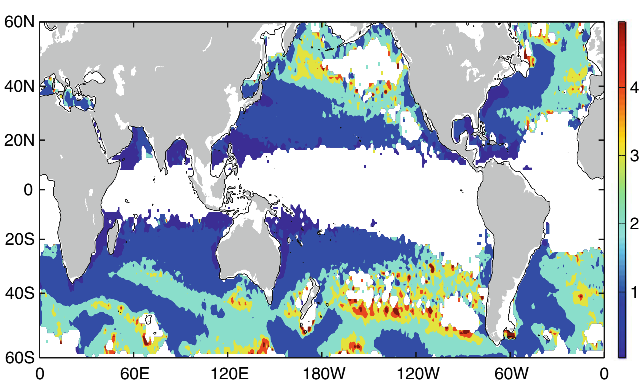

Fig. 5 The ratio of EAGPE/EKE whose resolution is $1\times1°$. The ratio larger than 5 is set to 5. The *black solid line* indicates the 200-m isobath

1.46 EJ (Huang 2010). Since most kinetic energy is in forms of eddy, this number can be used as an estimate of EKE. Ferrari and Wunsch (2009) put the estimate as 2.6 EJ, without giving the detail of their estimate. The large difference between EKE diagnosed in the present study is about ten times smaller than the values diagnosed from numerical model of data assimilation in the SODA data.

The total EAGPE in the world oceans remains unclear. Early estimate, such as Oort et al. (1994), of AGPE in the world oceans was based on dynamical framework of mesoscale dynamics. As discussed by Huang (2010), using such a formulation is, however, not suitable for the study of basin-scale circulation. A more accurate formulation gave the estimate of AGPE at 1,880 EJ (Huang 2005). However, the contribution due to the available internal energy is negative, and the algebraic sum of these two terms is 810 EJ. As discussed above, a suitable choice of referenced state is of critical importance in calculating the AGPE. For the study of eddy energetics, a reference state obtained by averaging the stratification within a horizontal domain on the order of the first deformation radius is a good choice,. The total amount of EAGPE in the world oceans sensitively depends on the choice of the reference state. Using either a $1\times1°$ or $2\times2°$ gird, the total amount of EAGPE in the world ocean was estimated at 1–8 EJ (Feng et al. 2006). These numbers are larger than the value of 0.224 EJ obtained in this study.

Thus, it is clear both the EKE and EAGPE estimates obtained in this study is much smaller than estimates obtained from theory and numerical models. In particular, EKE is one order of magnitude smaller than that obtained from numerical simulations. The large difference between our estimates and those from theory and numerical models may be due to the rather low spatial and horizontal resolutions used in collecting satellite data and the smoothing used in merging and analyzing the satellite data.

4.3 The mean generation/dissipation rate of mesoscale eddies

The generation/dissipation of mesoscale eddies is a key component of the general circulation because eddies take energy from the large-scale mean state through barotropic and baroclinic instability. Eventually, eddies dissipate their energy through many dynamical processes. However, most of these processes remain unclear at present time, and these processes are simply treated as either a net growth or a net dissipation of an eddy between two stations which the eddy occupied during the consequent time at two consequent time steps.

For eddies with lifetime ≥2 weeks, the annual mean generation/dissipation rate of eddy energy was calculated based on the Eqs. 10 and 11, Fig. 6. At the resolution

Table 1 Global sum of EKE and EAGPE diagnosed from satellite data and based on the equivalent two-layer model, in exajoules (10^{18} J)

Resolution used in smoothing		Cyclonic eddies	Anticyclonic eddies	Sum
6×6°	EKE	0.081	0.076	0.157
	EAGPE	0.113	0.111	0.224
	Sum	0.194	0.187	0.381
5×5°	EKE	0.044	0.041	0.085
	EAGPE	0.056	0.055	0.111
	Sum	0.100	0.096	0.196
7×7°	EKE	0.119	0.113	0.232
	EAGPE	0.174	0.171	0.345
	Sum	0.293	0.284	0.577

available from satellite data, the spatial distribution of the generation and dissipation rate is practically the same. In addition, the maps for cyclonic eddies and anticyclonic eddies are quite similar, and the minor difference can be seen only in the zonal integrated distribution shown in Fig. 7. Thus, only map of cyclonic eddy energy generation rate is presented here.

Comparing Fig. 6 with Fig. 1 indicates that eddies are abundant in the Kuroshio extension, the Gulf Stream extension and the ACC. In the Northern Hemisphere, high eddy activity appears in the West Boundary Current extensions, which seems directly linked to the instability of mean flow, with an energy generation rate on the order of 15 mW/m^2. The high-energy generation rate regime in the North Pacific Ocean appears as a zonal band, 30~42° N, but it extends further northeastward in the North Atlantic Ocean. In fact, one of the highest rate areas is located as far as 50^o N. This northeastward extension of high-energy generation rate seems directly linked to the strong eddy activity associated with the North Atlantic current.

In the Southern Hemisphere, the high-energy generation rate appears in the Brazil Current, the Brazil-Malvinas confluence (the recirculation in the Argentine basin), and the Agulhas Current and its retroflection. The corresponding currents and associated recirculation systems in the South Pacific Ocean do not appear as regimes of strong eddy generation. The equatorial band and a vast regime in the east part of the North and South Pacific Ocean turn out to be a zone of very low eddy generation. Some of these low eddy generation locations, such as the equatorial band, may be partially due to the data processing standards used in our analysis. There is another band of high energy generation rate in the South Hemisphere, closely associated with the core of ACC, Fig. 6.

In addition, eddy energy generation rate along the eastern boundary of the Pacific and off the western coast of Australia is one order of magnitude higher than the corresponding value in the adjacent interior ocean, suggesting local wave-induced generation mechanism of eddy (Zamudio et al. 2007) and eddy may generate or dissipate their energy at continental margin via relatively weak baroclinic instability, eddy–eddy interaction or eddy-wave interaction.

The characters of the zonally/meridionally integrated mean generation rates of eddies are shown in Fig. 7. In the meridional direction, there are three latitudinal bands of strong eddy energy generation. The first band is located around 35–40° N, apparently linked to the recirculation of Gulf Stream and Kuroshio. The additional secondary peak around 50° N reflects the contribution due to the North Atlantic Current. The local maximum energy generation rate of 3.1 GW/° for cyclonic eddies locates at 38° N, and the maximum rate of 3.0 GW/° for anticyclonic eddies locates at 40° N. This slight difference in latitude band is because of the polarity of meanders of the Gulf Stream and Kuroshio extension, which are cyclonic on the south side of the flow and anticyclonic on the north side of the flow.

The generation rate in the equatorial band is extremely low. South of 20° S, eddy energy generation rate gradually increases and reaches a large amplitude around two bands of peak value, one close to 38° S and another one between 48° and 55° S.

From Fig. 7, it is clear that more than half of eddy energy is generated in the Southern Hemisphere, especially

Table 2 Global sum of EKE and AGPE, in exajoules (10^{18} J)

	Equivalent 2-layer model	Feng et al. (2006)		Huang (2005)	Huang (2010)	Ferrari and Wunsch (2009)
		1×1° grid	2×2° grid			
AGPE	0.224	1	8	1,880 (810)		
EKE	0.157				1.46	2.6

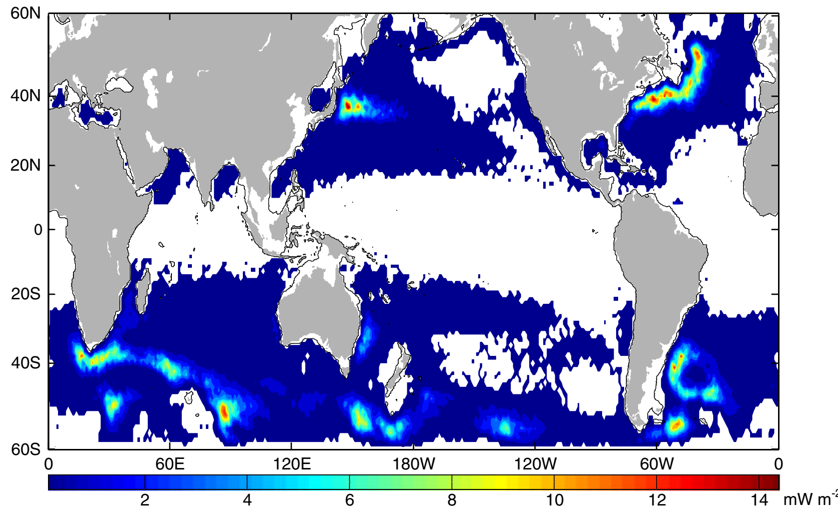

Fig. 6 The annual mean energy generation rate of cyclonic eddies with lifetimes ≥2 weeks, in milliWatts per square metre. The *black solid line* indicates the 200-m isobath

near ACC. The energy generation rate at the core of ACC reaches a value of 3.30 GW/° for cyclonic eddies and 3.16 GW/° for anticyclonic eddies at 48~56°S. At 156° E, contributions from the Kuroshio Extension and the confluence east of Australia give rise to a high peak of 1.18 GW/° for cyclonic eddies and 1.11 GW/° for anticyclonic eddies, lower panels of Fig. 7. The largest peaks appear near 48°W; in fact, the highest peak (1.46 GW/° for cyclonic eddies and 1.38 GW/° for anticyclonic eddies) is due to the contributions from the Gulf Stream Extensions and the Brazil-Malvinas confluence in the Argentine Basin. The smaller peaks at longitudes of 0~100° E result from the enhanced variability of eddy energy in the Agulhas Return Current and the ACC band.

It is clear that we must pay close attention to the link between local energy generation/dissipation and flow field and its interaction with topography. For example, the Luzon Strait is a narrow gap between the South China Sea and the Northwest Pacific. Wang et al. (2003) found that west of the Luzon Strait eddies are abundant. Our analysis indicates that this is a regime of relatively high eddy energy generation/dissipation rate. East of the Luzon Strait, Kuroshio is characterized by fast currents and strong shear. Strong eddy activity may be induced by the invasion of Kuroshio (Yuan et al. 2006). Moreover, the rough topography in the strait and the intense internal tides from the Pacific may also play a role in enhancing the eddy activity.

Likewise, intense currents and the rough bottom topography interact in the Yucatán Channel through which the Gulf Stream flows from the Caribbean Sea to the Gulf of Mexico, in the area that the ACC flows between the Falkland Islands and South Georgia and the South Sandwich Islands, and in the eastside of Australia where the East Australia Current exists, etc. The instability of mean flow results from the flow-topography interaction may enhance the local eddy generation rate. The annual

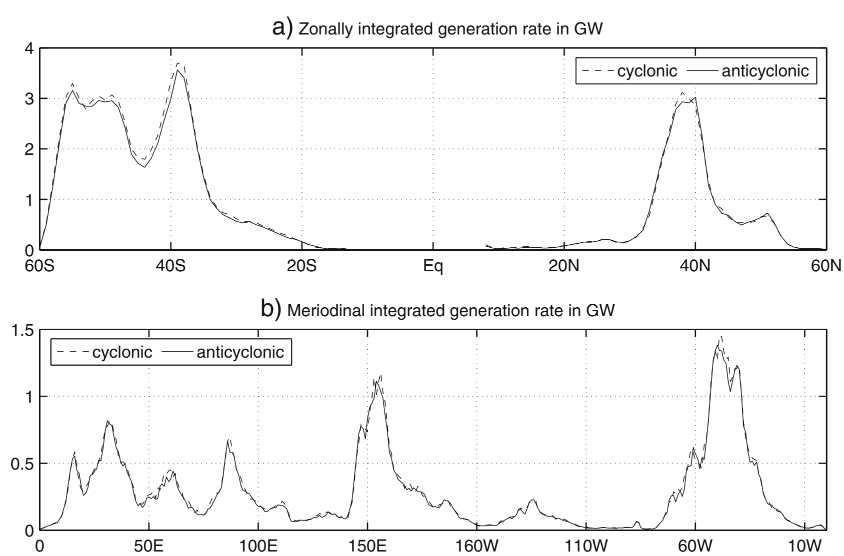

Fig. 7 The zonal (meridional) integration of global annual mean generation rate is shown in *top* (*bottom*), in gigaWatts per degree. *Solid line* indicates the annual mean generation rate of cyclonic eddies, *dashed line* indicates the annual mean generation rate of anticyclonic eddies

mean energy conversion rates in these regions are 2~6 times larger than those in the background (Figures not shown).

The total energy generation rate for mesoscale eddies with lifetime ≥2 weeks are listed in Table 3. The total generation/dissipation rate of mesoscale eddies is 0.203 TW, and the rate for cyclonic eddies is lower than that of anticyclonic eddies. It is important to notice that nearly half of eddy energy is generated in ACC. The eddy energy generated in the Northern Hemisphere is much lower than in the Southern Hemisphere.

As discussed above, eddy energy consists of two parts, EKE and EAGPE; both components take part in the energy transfer and conversion. According to the theory of baroclinic instability, at the horizontal scale of deformation radius, eddy energy is approximately equally partitioned between these two components. However, mesoscale eddies in the oceans gradually transfer their energy toward larger scale through eddy–eddy interaction. As scaling Eq. 34 revealed, at scale larger than the deformation radius, EAGPE is larger than EKE.

In many earlier studies the squared geostrophic velocity multiplied by a factor of 0.5 is treated as the EKE, without including the contribution of layer thickness. Furthermore, the EAGPE was seldom discussed. In view of the importance of eddy energy partition, we went through the calculation and separated these two components. In addition, the EKE component now contains the contribution due to the mass of each eddy. Hence, the generation rates of EKE and EAGPE for global cyclonic and anticyclonic eddies with lifetime ≥2 weeks are calculated (Fig. 8, top panel) and the global sums of these items are obtained (Table 4). Accordingly, for the EQ-model the EKE generation rate of cyclonic eddies is slightly lower than that of anticyclonic eddies. However, the EAGPE generation rate of cyclonic eddies is slightly higher than that of anticyclonic eddies. Further, like the ratio of EAGPE/EKE in Fig. 5, the ratio of cyclonic EAGPE generation rates over EKE generation rates is shown in Fig. 8 lower panel. For the global sums, in the EQ-model the EAGPE generation rate is about 1.3 times larger than that of EKE (Table 4).

As a comparison, we also include the results diagnosed from the TH-model (see details in Appendix 4). We believe that the results obtained from the EQ-model are more reliable, and thus our discussion in this paper is based on this model.

5 Summary and conclusions

By assuming the barotropic and first baroclinic modes have equal kinetic energy, the mean EKE and EAGPE are estimated at 0.157 and 0.224 EJ, and the mean generation/dissipation rate of mesoscale eddies is estimated at 0.2 TW. Previous estimates of the eddy generation and dissipation rate, such as Huang and Wang (2003) were based on rather crude eddy parameterization scheme. Due to the highly uncertainty of the parameters used in their estimation, the accurate value of this conversion remains unclear. In the latest review by Ferrari and Wunsch (2009), a value of 0.3 TW was assigned, but no details were available. To the best of our knowledge, no reliable estimate of eddy energy conversion rate obtained from numerical model has been reported. Thus, the value of 0.2 TW may be used as a target value.

The estimates of EKE and EAGPE reported in this study are much smaller than those obtained from theory and numerical simulations. In particular, EKE is at least 10 times smaller than the values based on theory and numerical simulation. Such major gaps are primarily due to the rather low spatial and temporal resolution of the altimetry data used in this study. Although the satellite altimetry data we used has a horizontal grid resolution of 0.333 deg by 0.265 deg, features can be resolved by this altimeter dataset are much coarser than this nominal resolution. As a reviewer pointed out that the large difference between our estimates and estimates based on theory and numerical simulations indicate that there are a lot of mesoscale and submesoscale eddies which were not resolved by this altimeter dataset. These smaller eddies may be responsible for a significant amount of eddy kinetic and available potential energy, which are not included in our estimates. Therefore, the EKE and EAGPE estimates in this study, as well as their generation/dissipation rates, should be interpreted as the lower bounds for the corresponding values. More accurate estimates for these important quantifies are clearly needed for further study. It is clear that revealing the important role of eddies in the ocean remains a grand challenge for observation technology, theory and numerical simulation.

Despite the large gaps between the estimates from this study and those based on theory and numerical simulations, many aspects of our results may be useful for understanding the role of eddies in the oceanic general circulation, such as the spatial patterns of the EKE and EAGPE distribution, the patterns of the generation/dissipation rate.

Although, a few estimates of eddy-related energy and conversion rates were reported in the literature, but they were poorly constrained, and not always consistent between each others. In particular, there were no estimates of EAGPE based on satellite observations. We postulated a theoretical framework of the calculation of EAGPE based on satellite SSHA observations. Thus, we believe that our estimates provide a set of consistent lower bounds for the eddy energetics in the world oceans based on satellite observations.

Table 3 Total generation/dissipation rate for eddies with lifetime ≥2 weeks, in gigaWatts

Model	Resolution used in smoothing	Eddy types	NH	SH	ACC	Global
Equivalent 2-layer model	6×6°	Cyclonic	32	71	49.7 (48.3%)	103
		Anticyclonic	32	68	47.4 (47.4%)	100
		Sum	64	139	97.1 (47.8%)	203
Thermocline model	6×6°	Cyclonic	29	29	12.0 (20.7%)	58
		Anticyclonic	28	27	11.0 (20.0%)	55
		Sum	57	56	23.0 (20.3%)	113
Equivalent 2-layer model	5×5°	Cyclonic	18	39	27.2 (47.7%)	57
		Anticyclonic	18	37	25.7 (46.7%)	55
		Sum	36	76	52.9 (47.2%)	112
Equivalent 2-layer model	7×7°	Cyclonic	46	104	72.1 (48.7%)	150
		Anticyclonic	45	99	68.5 (47.6%)	144
		Sum	91	203	52.9 (47.2%)	294

The percentages indicate the proportions of the part energy conversion rates by the total

NH Northern Hemisphere, *SH* Southern Hemisphere (including the ACC band), *ACC* zonal band from 40° S to 60° S

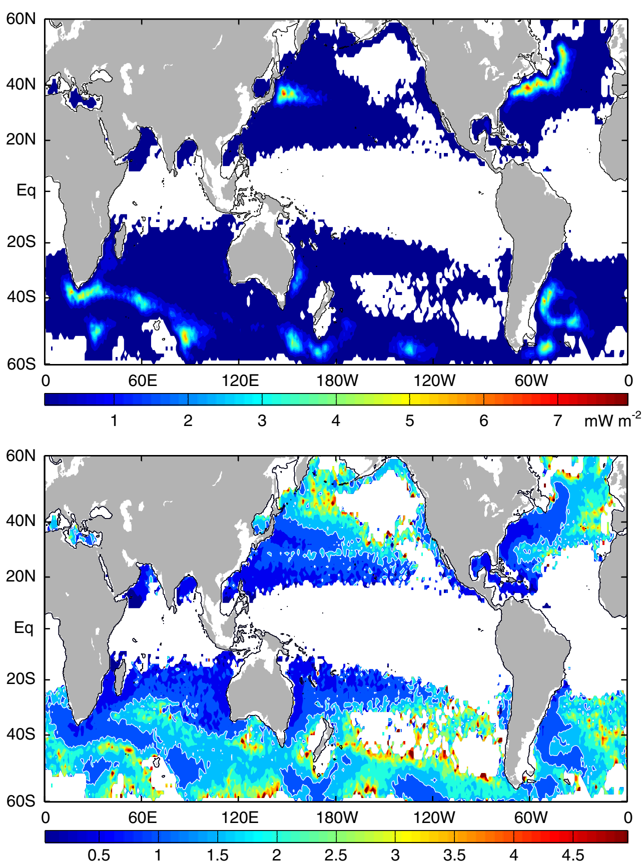

Fig. 8 *Top panel*, mean EKE generation rate for cyclonic eddies with lifetime ≥2 weeks, in milliWatts per square meter. *Lower panel*, the ratio of EAGPE generation rates for cyclonic eddies over their EKE generation rates. The *white thin line* indicates the contour that ratio equals 1.5, and the *black solid line* indicates the 200-m isobath

One of the major uncertainties in our analysis is the working assumption that EKE is equally participated between the barotropic mode and the first baroclinic mode. (If we assumed that all kinetic energy is in the form of the first baroclinic mode, the corresponding total eddy energy and its generation rate is estimated at 0.646 EJ and 0.345 TW, respectively, details of this analysis is not included). Although Wunsch (1997) and Forget and Wunsch (2007) suggested that most eddy energy on the sea surface is contained in the first baroclinic mode is a reasonable approximation, recent studies raised some questions about this assumption. For example, Lapeyre (2009) suggested that the SSHA signals may be dominated by the surface geostrophic solutions. However, the surface geostrophic solutions are surface trapped, and the corresponding interfacial displacement in the deep part of the ocean is quite small; thus, such surface trapped motions cannot be associated with a large amount of available potential energy. Accordingly, the rate of eddy energy generation and dissipation would be greatly reduced, and this may give rise to a completely different global energy balance. To resolve this critically important issue, further studies involving analyzing in situ observations or eddy-resolving numerical model output are necessary.

There is a great uncertainty associated with the choice of filtering scale because results obtained from processing satellite data are sensitive to the choice of filtering scale. Different filtering scales may give quite different results. We have carried out similar calculation using filtering scales from 5×5° to 7×7°, and the obtained eddy energy varies within the range of 0.196~0.577 EJ and energy generation rate varies within the range of 0.11~0.29 TW (Tables 1, 3, and 4).

Table 4 Global generation/dissipation rate for eddies with lifetimes ≥2 weeks, in gigaWatts

Model	Resolution used in smoothing	EKE			EAGPE			Total
		Cyclonic	Anticyclonic	Total	Cyclonic	Anticyclonic	Total	
Equivalent 2-layer model	6×6°	45	43	88	58	57	115	203
	5×5°	26	25	51	31	30	61	112
	7×7°	64	60	124	86	84	170	294
Thermocline model	6×6°	27	25	52	30	31	60	113

Our results suggest that most of eddy energy dissipation takes place in the middle of the wind-driven circulation, especially the recirculation regimes and the ACC. The regimes of strong dissipation in the Northern Hemisphere do not seem to be directly linked to the bottom topography. Thus, energy dissipation through interaction with bottom topography may not be the only way to dissipate eddy energy. Other mechanisms, such as dissipation through loss of balance and interacting with the atmosphere may play some kind of role.

Acknowledgments This study used altimeter data available by the AVISO Altimetry Operations Center, plus hydrographic data World Ocean Atlas 2001 provided by the US National Oceanographic Data Center. Reviewers' critical comments helped us improving the presentation of this paper. This study is supported by grants KZCX1-YW-12-02, 40976010, 40776008, and U1033002.

Appendix 1: Formulation based on a two-layer model

A first-baroclinic-mode eddy can be examined in terms of a two-layer model, Fig. 9, where η is the sea level anomaly, h_1 is the depth of the interface, d is the interfacial disturbance, (H_1 and H_2), (u_1 and u_2), and (ρ_1 and ρ_2) are the mean thickness, horizontal velocity, and density of the upper and lower layers. The corresponding pressure gradient in each layer is

$$\begin{aligned}\nabla p_1 = g\rho_1\nabla\eta, \nabla p_2 &= g\rho_1\nabla\eta - g\Delta\rho\nabla h_1 \\ &= g\rho_1\nabla\eta - g\Delta\rho\nabla d,\end{aligned} \tag{14}$$

where g is the gravitational acceleration, $\Delta\rho = \rho_2 - \rho_1$ is the density difference between the upper and lower layers. These relations can be rewritten as

$$\frac{\nabla p_1}{\rho_1} = g\nabla\eta, \frac{\nabla p_2}{\rho_2} \approx g\nabla\eta - g'\nabla d, \tag{15}$$

where $g' = g\Delta\rho/\rho_2$ is the reduced gravity. Geostrophic velocity in each layer is proportional to the pressure gradient, the right panel of Fig. 9. By definition, volumetric transport in each layer should satisfy the following constraint

$$u_1H_1 + u_2H_2 = 0. \tag{16}$$

From these equations we obtain

$$d = \frac{g}{g'}\left(1 + \frac{H_1}{H_2}\right)\eta. \tag{17}$$

Thus, the horizontal pressure term in the lower layer is reduced to

$$\frac{\nabla p_2}{\rho_2} \approx -g\frac{H_1}{H_2}\nabla\eta = -\frac{H_1}{H_2}\frac{\nabla p_1}{\rho_1}. \tag{18}$$

When the lower layer is much thicker than the upper layer, velocity in the lower layer is much smaller than that of the upper layer; however, the volumetric transport in the lower layer is not negligible because it is exactly the same as that in the upper layer (with an opposite sign).

In the present two-layer model, if the lower layer is much thicker than the upper layer, the layer ratio term in Eq. 17 can be omitted, and the corresponding expression is reduced to

$$d \approx \frac{g}{g'}\eta. \tag{19}$$

However, in our calculation, the exact expression 17 for our two-layer approximation of the stratification is used.

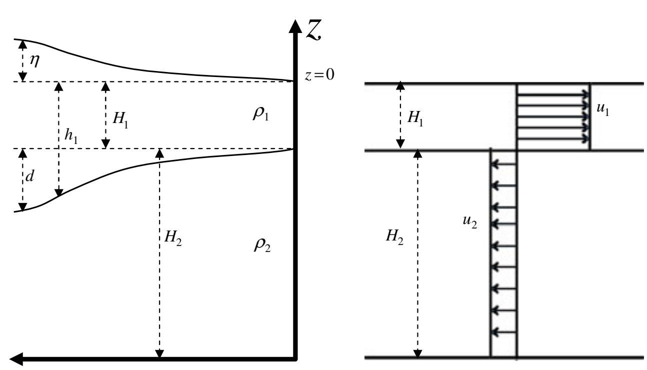

Fig. 9 Sketch of the free surface and the layer interface in a two-layer model: *left panel*, free surface and interface of a two-layer model. *Right panel*, velocity pattern of the first baroclinic mode. The *symbols* are explained in the main text

The AGPE for a two-layer model can be calculated as follows. Assume the undisturbed upper layer thickness is H_1, the free surface elevation is η and the interface depression is d, Fig. 10. The reference state is defined as the state with minimal gravitational potential energy, which corresponds to a state with both the free surface and the interfacial surface leveled off, as shown by the dashed horizontal lines in Fig. 10. Since the vertical movement involved is very small, we assume that water density does not change with pressure. As a result, the only changes are as follows. Firstly, the free surface elevation anomaly is flatted out, as shown by the arrow in the upper part of Fig. 10. Secondly, the interface is flatted out, indicated by the solid arrow in the lower part of Fig. 10. However, other parts of upper and lower layer remain unchanged.

The calculation of AGPE is separated into two parts. For the upper part of the water column, we use the upper surface of the undisturbed upper layer as the reference state. The total gravitational potential energy of the water parcel before and after adjustment is

$$\chi^0_{\mathrm{Top}} = \frac{g\rho_1 b}{2}\eta^2, \tag{20}$$

$$\chi^1_{\mathrm{Top}} = \frac{g\rho_1}{2}(B+b)a^2 = \frac{g\rho_1}{2}\frac{b^2}{B+b}\eta^2. \tag{21}$$

Thus, the corresponding available gravitational potential energy is

$$\Delta\chi_{\mathrm{Top}} = \chi^0_{\mathrm{Top}} - \chi^1_{\mathrm{Top}} = \frac{g\rho_1}{2}\frac{Bb}{B+b}\eta^2. \tag{22}$$

For the lower part of the water column near the interface, there are two water parcels exchanging their positions. For simplicity, we use the non-disturbed interface as the reference level. Before the adjustment, the total gravitational potential energy for the upper layer parcel (on the lower left corner) and the lower layer (on the lower right corner) is

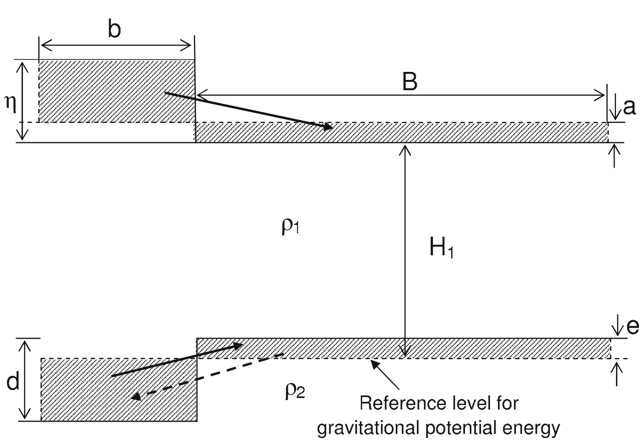

Fig. 10 Water parcel movement during the adjustment to a state of minimal gravitational potential energy

$$\chi^0_{\mathrm{Bot},1} = -\frac{g\rho_1}{2}b(d-e)^2, \tag{23}$$

$$\chi^0_{\mathrm{Bot},2} = \frac{g\rho_2}{2}Be^2. \tag{24}$$

The corresponding terms after adjustment have similar expressions,

$$\chi^1_{\mathrm{Bot},1} = \frac{g\rho_1}{2}Be^2, \tag{25}$$

$$\chi^1_{\mathrm{Bot},2} = -\frac{g\rho_2}{2}b(d-e)^2. \tag{26}$$

Thus, the available gravitational potential energy associated with the adjustment of these two water parcels are

$$\begin{aligned}\Delta\chi_{\mathrm{Bot}} &= \chi^0_{\mathrm{Bot},1} + \chi^0_{\mathrm{Bot},2} - \chi^1_{\mathrm{Bot},1} - \chi^1_{\mathrm{Bot},2} \\ &= \frac{g\Delta\rho}{2}\frac{bB}{(B+b)}d^2.\end{aligned} \tag{27}$$

For an individual eddy, the width of the background stratification field is much larger than the width of the eddy, so that$B \gg b$, and the corresponding total available gravitational potential energy for the unit length, obtained by dividing the width of b, is

$$\chi = \Delta\chi_{\mathrm{Top}} + \Delta\chi_{\mathrm{Bot}} \approx \frac{g\Delta\rho}{2}d^2 + \frac{g\rho_1}{2}\eta^2. \tag{28}$$

Using Eq. 17, this is reduced to

$$\chi \approx \frac{g\Delta\rho}{2}\left[1 + \frac{g'}{g}\left(\frac{H_2}{H_1+H_2}\right)^2\right]d^2. \tag{29}$$

Since the reduced gravity is much smaller than gravity, the second term in Eq. 29 is negligible and the total available gravitational potential energy per unit length is

$$\chi \approx \frac{g\Delta\rho}{2}d^2. \tag{30}$$

Our discussion above can be extended to the case of an eddy in a cylindrical coordinates. Assuming eddy dimension is much smaller than the dimension of the ocean, the results are the same.

The ratio of EAGPE and EKE for an eddy is estimated as follows. The geostrophic velocity of an eddy in the upper layer is estimated as

$$u_1 = g|\nabla\eta|/f \approx g\eta_{\max}/fr, \tag{31}$$

where $f= 2\Omega\sin\theta$ is the Coriolis parameter, Ω is the earth rotation rate, θ is the latitude, $\eta_{\max}$ is the maximal free surface elevation at the center of the eddy and r is the radius of the eddy. Therefore, the total amount of kinetic energy of an eddy integrated over the total area of the eddy, A, is estimated as

$$E_k = \frac{1}{2}\rho_1 H_1\left(1+\frac{H_1}{H_2}\right)\iint_A u^2 \mathrm{d}A \approx \frac{1}{2}\rho_1 H_1\left(1+\frac{H_1}{H_2}\right)\left(\frac{g\eta_{\max}}{fr}\right)^2 A. \quad (32)$$

The corresponding total available gravitational potential energy of an eddy is estimated as

$$E_{\text{agpe}} \approx \frac{1}{2}\Delta\rho g\left[\frac{g}{g'}\left(1+\frac{H_1}{H_2}\right)\eta_{\max}\right]^2 A. \quad (33)$$

Thus, the ratio of these two types of energy for an eddy is

$$R = \frac{E_{\text{agpe}}}{E_k} \approx \left(\frac{r}{r_d}\right)^2, \quad (34)$$

where $r_d = \sqrt{g' H_1 H_2/(H_1+H_2)}/f$ is the first radius of deformation. Thus, for eddy with radius close to the first deformation radius, the total energy is roughly equally partitioned between the EAGPE and EKE. However, most eddies identifiable from the oceanic datasets, especially from the altimetry, the horizontal length scale is much larger than the first radius of deformation (Chelton et al. 2007a; Stammer, 1997; Roemmich and Gilson, 2001). As a result, the eddy energy is mostly in the form of EAGPE.

Appendix 2: Inferring the two-layer model from a continuously stratified model

A vitally important step in formulating the two-layer model is to specify the equivalent depth of the mean interface and the density difference between the two layers. A simple approach is to use the depth of the main pycnocline and the associated density jump. In the following discussion this model will be called the thermocline model (TH-model). Such a model is, however, not suitable for the subpolar basin and the Southern Ocean where the main thermocline is poorly defined.

A better approach in parameterization of a two-layer model was described by Flierl (1978). Mesoscale eddy can be described in terms of the normal modes, and the standard formulation has been described in many previous literatures, e.g., Pedlosky (1987), Chelton et al. (1998), and Huang and Pedlosky (2002). Our notation here follows Flierl (1978). The normal modes can be defined as the following eigen value/function problem:

$$\frac{\mathrm{d}}{\mathrm{d}z}\left(\frac{f^2}{N^2}\frac{\mathrm{d}F_n}{\mathrm{d}z}\right) + \lambda_n F_n = 0, \quad (35a)$$

$$\frac{\mathrm{d}F_n}{\mathrm{d}z} = 0, z = 0, -H, \quad (35b)$$

where $F_n(z)$ is the nth eigen mode,λ_n is the corresponding eigen value, N^2 is the squared buoyancy frequency, and H is the depth of the sea floor. A normalization constraint is also applied to the eigen functions

$$\int_{-H}^{0} F_i F_j \mathrm{d}z = H\delta_{ij}. \quad (36)$$

Our study is focused on the first baroclinic mode. The choice of parameter for a two-layer model depends on the physical aspects of the problem as discussed by Flierl (1978). Unfortunately, no suitable formulation specifically designed for the study of the available potential energy is available at present time; thus, we will adapt the standard formulation for normal mode presented by Flierl (1978). Accordingly, the equivalent interface depth and the equivalent density step are

$$H_1 = \frac{H}{1+F_1^2(0)}, \quad (37)$$

$$\varepsilon = \frac{f_0^2 H}{\lambda_1 g H_1 (H-H_1)}. \quad (38)$$

The equivalent reduced gravity is defined as

$$g' = \varepsilon g. \quad (39)$$

This model will be called the equivalent two-layer model (EQ-model).

Appendix 3: Calculation of the annual mean generation/dissipation rate of mesoscale eddies

Through eddy identification and tracking, the time series of position and energy for an eddy were obtained and the total energy of an eddy at each moment during its lifetime were calculated as summation of EKE and EAGPE. The detailed algorithm of annual mean generation and dissipation rate of the mesoscale eddy is as follows.

Assume that we have a time series of an eddy, including its position and the SSHA at time $t = t_1, t_2, \ldots, t_{n-1}$ with uniform time step of 1 week. In order to analyze the life cycle of an eddy, we need to define the beginning and end of the eddy. The beginning of an eddy is with zero energy, so that $e_0 = 0$, and its time is defined as $t_0 = -2t_1 + t_2$; its position is defined by a linear extrapolation from points 1 and 2: $(x_0, y_0) = (-2x_1 + x_2, -2y_1 + y_2)$. Similarly, the end of the eddy can be defined.

The energy source or sink within each pair of points $de_{i,i+1}$ is calculated as

$$de_{01} = e_1 - e_0 = e_1, \tag{41}$$

$$de_{i,i+1} = e_{i+1} - e_i, \tag{42}$$

The location of $de_{i,i+1}$ is in the middle of these two positions.

Gridded energy variation data set was required, so the $1 \times 1°$ grid was chosen here. Suppose we have four grid points: (i, j), $(i+1, j)$, $(i, j+1)$, $(i+1, j+1)$, the contributions to four grid points were calculated by the method of weighting. We assume there is a point source de locates (m and n) with a non-dimensional position (X and Y) within this grid net, $X=m-i$, $Y=n-j$. Thus, contribution of this source to the grid points at the four comers is:

$$e(i,j) = \mathrm{d}e(1-X)(1-Y), \tag{43}$$

$$e(i+1,j) = \mathrm{d}eX(1-Y), \tag{44}$$

$$e(i,j+1) = \mathrm{d}e(1-X)Y, \tag{45}$$

$$e(i+1,j+1) = \mathrm{d}eXY. \tag{46}$$

As a result, in 15-year accumulation the total contribution of these sources or sinks at those grid points is:

$$E_{i,j}^{\mathrm{source}} = \sum_{n=1,\mathrm{for}\, e_n>0}^{N} e_n, \tag{57}$$

$$E_{i,j}^{\mathrm{sink}} = \sum_{n=1,\mathrm{for}\, e_n<0}^{N} e_n. \tag{48}$$

The total contribution of these sources or sinks at each grid point divided by the 15-year time is the annual mean generation and dissipation rate of mesoscale eddies:

$$w_{i,j}^{\mathrm{source}} = E_{i,j}^{\mathrm{source}}/T, \tag{49}$$

$$w_{i,j}^{\mathrm{sink}} = E_{i,j}^{\mathrm{sink}}/T. \tag{50}$$

Appendix 4: Results in TH-model

Results from the TH-model are much smaller than the corresponding values obtained from the EQ-model, and the global sum of eddy energy generation rate is estimated at 0.113 TW (Table 3). In particular, the contribution from the ACC in the EQ-model is also much higher than that obtained from the TH-model. Such difference is due to the fact that the TH-model underestimates both the depth of the equivalent interface and the density jump across the interface, as shown in Figs. 2 and 3.

Accordingly, for the TH-model the EKE generation rate of cyclonic eddies is slightly lower than that of anticyclonic eddies. However, the EAGPE generation rate of cyclonic eddies is slightly higher than that of anticyclonic eddies. For the global sums, in the TH-model the EAGPE generation rate is 1.15 times larger than that of EKE (Table 4).

Since the interface depth in the TH-model is not suitable for the eddy in the subpolar basin and the Southern Ocean where the main thermocline is poorly defined, we present the results from the TH-model as a comparison and a sensitivity test.

References

Arbic BK, Flierl GR (2004) Baroclinically unstable geostrophic turbulence in the limits of strong and weak bottom Ekman friction: application to midocean eddies. J Phys Oceanogr 34:2257–2273. doi:10.1175/1520-0485(2004)034<2257:BUGTIT>2.0.CO;2

Arbic BK, Shriver JF, Hogan PJ, Hurlburt HE, McClean JL, Metzger EJ, Scott RB, Sen A, Smedstad OM, Wallcraft AJ (2009) Estimates of bottom flows and bottom boundary layer dissipation of the oceanic general circulation from global high-resolution models. J Geophys Res 114:C02024. doi:10.1029/2008JC005072

Carton JA, Giese BS (2008) A reanalysis of ocean climate using Simple Ocean Data Assimilation (SODA). Mon Weather Rev 136:2999–3017. doi:10.1175/2007MWR1978.1

Chelton DB, Schlax MG (1996) Global observations of oceanic Rossby waves. Science 272:234–238. doi:10.1126/science.272.5259.234

Chelton DB, De Szoeke RA, Schlax MG (1998) Geographical variability of the first baroclinic Rossby radius of deformation. J Phys Oceanogr 28:433–460. doi:10.1175/1520-0485(1998)028<0433:GVOTFB>2.0.CO;2

Chelton DB, Schlax MG, Samelson RM, de Szoeke RA (2007a) Global observations of large oceanic eddies. Geophys Res Lett 34:L15606. doi:10.1029/2007GL030812

Chelton, D. B., M. G. Schlax, R. M. Samelson, and R. A. de Szoeke (2007b) Global observations of westward energy propagation in the ocean: Rossby waves or nonlinear eddies? Fall Meet. Suppl. abstract #OS13E-07, AGU Fall Meeting, 87(52), San Francisco, CA, USA.

Cheney RE, Marsh JG, Beckley BD (1983) Global mesoscale variability from collinear tracks of SEASAT altimeter data. J Geophys Res 88:4343–4354. doi:10.1029/JC088iC07p04343

Ducet N, Le Traon PY, Reverdin G (2000) Global high-resolution mapping of ocean circulation from TOPEX/Poseidon and ERS-1 and -2. J Geophys Res 105:19,477–19,498. doi:10.1029/2000JC900063

Feng Y, Wang W, Huang RX (2006) Mesoscale available gravitational potential energy in the world oceans. Acta Oceanolog Sin 25:1–13

Ferrari R, Wunsch C (2009) Ocean circulation kinetic energy: reservoirs, sources, and sinks. Annu Rev Fluid Mech 41:253–282. doi:10.1146/annurev.fluid.40.111406.102139

Ferrari R, Wunsch C (2010) The distribution of eddy kinetic and potential energy in global ocean. Tellus Ser A 62:92–108. doi:10.1111/j.1600-0870.2009.00432.x

Flierl GR (1978) Models of vertical structure and calibration of 2-layer models. Dyn Atmos Oceans 2:341–381. doi:10.1016/0377-0265(78)90002-7

Forget G, Wunsch C (2007) Estimated global hydrographic variability. J Phys Oceanogr 37:1997–2008. doi:10.1175/JPO03072.1

Frankignoul C, Muller P (1979) Quasi-geostrophic response of an infinite beta-plane ocean to stochastic forcing by the atmosphere. J Phys Oceanogr 9:104–127. doi:10.1175/1520-0485(1979)009<0104:QGROAI>2.0.CO;2

Fu L, Keffer T, Niiler P, Wunsch C (1982) Observations of mesoscale variability in the western North Atlantic: a comparative study. J Mar Res 40:809–848

Gill AE, Green JSA, Simmons AJ (1974) Energy partition in the large-scale ocean circulation and the production of mid-ocean eddies. Deep Sea Res 21:499–528. doi:10.1016/0011-7471(74)90010-2

Gille S, Yale M, Sandwell D (2000) Global correlation of mesoscale ocean variability with seafloor roughness from satellite altimetry. Geophys Res Lett 27:1251–1254. doi:10.1029/1999GL007003

Gould WJ, Schmitz WJ Jr, Wunsch C (1974) Preliminary field results for a Mid-Ocean Dynamics Experiment (MODE-0). Deep Sea Res 21:911–931. doi:10.1016/0011-7471(74)90025-4

Huang RX (2005) Available potential energy in the world's oceans. J Mar Res 63:141–158. doi:10.1357/0022240053693700

Huang RX (2010) Ocean circulation, wind-driven and thermohaline processes. Cambridge University Press, Cambridge, p 806

Huang RX, Pedlosky J (2002) On aliasing Rossby waves induced by asynchronous time stepping. Ocean Model 5:65–76. doi:10.1016/S1463-5003(02)00014-8

Huang, R. X., and W. Wang (2003) Gravitational potential energy sinks in the oceans, Near-boundary processes and their parameterization. In: Proceedings, Hawaii winter workshop. pp 239–247.

Huang RX, Wang W, Liu LL (2006) Decadal variability of wind-energy input to the world ocean. Deep-Sea Research, Part II 53:31–41

Killworth PD, Blundell JR (2007) Planetary wave response to surface forcing and instability in the presence of mean flow and topography. J Phys Oceanogr 37:1297–1320

Lapeyre G (2009) What vertical mode does the altimeter reflect? On the decomposition in baroclinic modes and on a surface-trapped mode. J Phys Oceanogr 39:2857–2874. doi:10.1175/2009JPO3968.1

Oort AH, Anderson LA, Peixoto JP (1994) Estimates of the energy cycle of the oceans. J Geophys Res 99:7665–7688. doi:10.1029/93JC03556

Pedlosky J (1987) Geophysical Fluid Dynamics. Springer, New York, p 710

Richardson PL (1983) Eddy kinetic energy in the North Atlantic from surface drifters. J Geophys Res 88:4355–4367. doi:10.1029/JC088iC07p04355

Roemmich D, Gilson J (2001) Eddy transport of heat and thermo-cline waters in the North Pacific: a key to interannual/decadal climate variability? J Phys Oceanogr 31:675–687. doi:10.1175/1520-0485(2001)031<0675:ETOHAT>2.0.CO;2

Scott R, Xu Y (2009) An update on the wind power input to the surface geostrophic flow of the World Ocean. Deep Sea Res I 56:295–304. doi:10.1016/j.dsr.2008.09.010

Sen A, Scott R, Arbic B (2008) Global energy dissipation rate of deep-ocean low-frequency flows by quadratic bottom boundary layer drag: computations from current-meter data. Geophys Res Lett 35:L09606. doi:10.1029/2008GL033407

Shum CK, Werner RA, Sandwell DT, Zhang BH, Nerem RS, Tapley BD (1990) Variations of global mesoscale eddy energy observed from GEOSAT. J Geophys Res 95:17865–17876. doi:10.1029/JC095iC10p17865

Smith K (2007) The geography of linear baroclinic instability in Earth’s oceans. J Mar Res 65:655–683. doi:10.1357/002224007783649484

Stammer D (1997) Global characteristics of ocean variability estimated from regional TOPEX/POSEIDON altimeter measurements. J Phys Oceanogr 27:1743–1769. doi:10.1175/1520-0485(1997)027<1743:GCOOVE>2.0.CO;2

Stammer D, Boning C, Dieterich C (2001) The role of variable wind forcing in generating eddy energy in the North Atlantic. Prog Oceanogr 48:289–311. doi:10.1016/S0079-6611(01)00008-8

Wang G, Su J, Chu P (2003) Mesoscale eddies in the South China Sea observed with altimeter data. Geophys Res Lett 30:2121. doi:10.1029/2003GL018532

Wunsch C (1997) The vertical partition of oceanic horizontal kinetic energy. J Phys Oceanogr 27:1770–1794. doi:10.1175/1520-0485(1997)027<1770:TVPOOH>2.0.CO;2

Wunsch C (1998) The work done by the wind on the oceanic general circulation. J Phys Oceanogr 28:2332–2340. doi:10.1175/1520-0485(1998)028<2332:TWDBTW>2.0.CO;2

Wunsch C (2007) The past and future ocean circulation from a contemporary perspective, Ocean circulation: mechanisms and impacts: past and future changes of meridional overturning. Geophysical Monograph-American Geophysics Union 173:53–74

Wunsch C, Ferrari R (2004) Vertical mixing, energy and the general circulation of the oceans. Ann Rev Fluid Mech 36:281–314. doi:10.1146/annurev.fluid.36.050802.122121

Wyrtki K, Magaard L, Hager J (1976) Eddy Energy in the Oceans. J Geophys Res 81:2641–2646. doi:10.1029/JC081i015p02641

Yuan D, Han W, Hu D (2006) Surface Kuroshio path in the Luzon Strait area derived from satellite remote sensing data. J Geophys Res 111:C11007. doi:10.1029/2005JC003412

Zamudio L, Hurlburt HE, Metzger EJ, Tilburg CE (2007) Tropical wave-induced oceanic eddies at Cabo Corrientes and the María Islands Mexico. J Geophys Res 112:C05048. doi:10.1029/2006JC004018

Zlotnicki V, Fu LL, Patzert W (1989) Seasonal variability in global sea level observed with geosat altimetry. J Geophys Res 94:17959–17969. doi:10.1029/JC094iC12p17959